Perovich, D, et al. 2025. Theoretical estimates of light transmittance at the MOSAiC Central Observatory. *Elem Sci Anth*, 13: 1.
DOI: https://doi.org/10.1525/elementa.2024.00076

RESEARCH ARTICLE

Theoretical estimates of light transmittance at the MOSAiC Central Observatory

Don Perovich[1,*], Bonnie Light[2], Madison M. Smith[3], Melinda Webster[2], Marika M. Holland[4], David Clemens-Sewall[4,5], Ian A. Raphael[1], Chris Polashenski[1,6], Andrew P. Barrett[7], Christopher J. Cox[5], Polona Itkin[8], Felix Linhardt[9], Amy R. Macfarlane[10,11,12], Marcel Nicolaus[13], Natascha Oppelt[9], Matthew D. Shupe[14], Julienne Stroeve[7,15], and Ran Tao[13]

Light transmission through a sea ice cover has strong implications for the heat content of the upper ocean, the magnitude of bottom and lateral ice melt, and primary productivity in the ocean. Light transmittance in the vicinity of the Multidisciplinary Drifting Observatory for the Study of Arctic Climate (MOSAiC) Central Observatory was estimated by driving a two-stream radiative transfer model with physical property observations. Data include point and transect observations of snow depth, surface scattering layer thickness, ice thickness, and pond depth. The temporal evolution of light transmittance at specific sites and the spatial variability along transect lines were computed. Ponds transmitted 4–6 times as much solar energy per unit area as bare ice. On July 25, ponds covered about 18% of the area and contributed roughly 50% of the sunlight transmitted through the ice cover. Approximating the transmittance along a transect line using average values for the physical properties will always result in lower light transmittance than finding the average light transmittance using the full distribution of points. Transmitted solar energy calculated using the standard five ice thickness categories and three surface types used in the Los Alamos sea ice model CICE, the sea ice component of many weather and climate models, was only about 1 W m^{-2} less than using all the points along the transect. This minor difference suggests that the important processes and resulting feedbacks relating to solar transmittance can be represented in models that use five or more categories of ice thickness distributions.

Keywords: Sea ice, Light transmittance variability, Optical properties

Introduction

Understanding the interaction of sunlight with the Arctic sea ice cover is of prime importance for several reasons. The ice albedo feedback has climate significance beyond the Arctic, in part due to its strong role in amplifying the observed temperature change in the Arctic relative to the rest of the globe (Rantanen et al., 2022). In spring and summer, solar radiation is a major term in the surface heat budget of the ice and therefore plays a central role in annual sea ice melt. Light transmitted through the sea ice cover influences solar heating of the ocean and primary productivity within the ice and upper ocean (Stroeve et al., 2024).

Because of these important considerations, optical measurements have long been a part of field experiments and remote sensing efforts. The spatial variability and temporal evolution of albedo have been measured extensively

---

[1] Thayer School of Engineering, Dartmouth College, Hanover, NH, USA

[2] Polar Science Center, Applied Physics Laboratory, University of Washington, Seattle, WA, USA

[3] Woods Hole Oceanographic Institution, Woods Hole, MA, USA

[4] Climate and Global Dynamics Laboratory, NSF National Center for Atmospheric Research, Boulder, CO, USA

[5] National Oceanic and Atmospheric Administration Physical Sciences Laboratory and Climate and Global Dynamics Laboratory, Boulder, CO, USA

[6] USACE-Cold Regions Research and Engineering Laboratory, Hanover, NH, USA

[7] National Snow and Ice Data Center, University of Colorado, Boulder, CO, USA

[8] Norwegian Polar Institute, Tromso, Norway

[9] Department of Geography, Kiel University, Kiel, Germany

[10] UiT The Arctic University of Norway, Tromso, Norway

[11] Northumbria University, Newcastle, UK

[12] WSL Institute for Snow and Avalanche Research SLF, Davos, Switzerland

[13] Alfred-Wegener-Institut Helmholtz-Zentrum für Polar- und Meeresforschung, Bremerhaven, Germany

[14] Cooperative Institute for Research in Environmental Sciences, University of Colorado and NOAA Physical Sciences Laboratory, Boulder, CO, USA

[15] University of Manitoba, Winnipeg, MB, Canada

* Corresponding author:
Email: donald.k.perovich@dartmouth.edu

from the surface (Light et al., 2022; Perovich et al., 2002), from aircraft, and from satellites (Pohl et al., 2020; Riihelä et al., 2021). Measurements of light transmission through the ice are more difficult to make and are fewer in number than albedo measurements. Less is known about the temporal evolution and spatial variability of transmission. Light transmission measurements have been made at individual sites (Light et al., 2008; 2015), along remotely operated vehicle (ROV) survey lines (Nicolaus et al., 2012; Nicolaus and Katlein, 2013; Katlein et al., 2015; 2019), and using autonomous instruments (Wang et al., 2014; Tao et al., 2024). Stroeve et al. (2024) combined satellite-derived ice properties with a radiative transfer model to calculate large scale estimates of the under-ice light field.

Various light transmission measurements were made during the Multidisciplinary Drifting Observatory for the Study of Arctic Climate (MOSAiC) field campaign, a drift experiment conducted in the central Arctic Ocean from September 2019 to October 2020 (Nicolaus et al., 2022). A series of spectral transmission surveys was made from an ROV (Nicolaus et al., 2022), and a time series of spectral transmission was made at several autonomous stations (Rabe et al., 2024; Tao et al., 2024). There were also extensive measurements of the physical properties of the ice cover (e.g., Itkin et al., 2023), including snow depth, ice thickness, and melt pond depth. Albedo measurements were made from the surface (Light et al., 2022), from drones (Calmer et al., 2023), and from aircraft (Patzold et al., 2023; Jäkel et al., 2024).

In this paper, we explore the spatial variability and temporal evolution of light transmission under second year ice by combining physical property measurements with a two-stream radiative transfer model. Spatial variability and seasonal differences in transmittance are discussed. Estimates of photosynthetically available radiation and of solar heating of the upper ocean are presented.

Approach

The spatial variability and temporal evolution of spectral transmittance were investigated by combining a radiative transfer model with a time series of snow depth and ice thickness measured at a single point and with extensive surveys of ice thickness and surface properties. There are several different sea ice radiative transfer models using different approaches and levels of complexity (Grenfell, 1991; Light et al., 2003; Briegleb and Light, 2007; Stamnes et al., 2018). In this study, a two-stream, spectral, radiative transfer model was used (Perovich, 1990; 2005). The model is simple computationally and can treat multiple layers with different inherent optical properties. The model calculates the spectral transmittance ($T(\lambda)$) every 10 nm of wavelength (λ) from 400 nm to 1000 nm. The spectral transmittance is the fraction of the incident irradiance at the surface ($E(\lambda)$) that is transmitted through the ice ($t(\lambda)$):

$$T(\lambda) = t(\lambda)/E(\lambda).$$

Little, if any, sunlight is transmitted through sea ice at wavelengths beyond 1000 nm because of the large absorption coefficients associated with pure ice and water at these wavelengths.

The model includes spectral incident irradiance ($E(\lambda)$) for four different sky conditions, ranging from clear skies to completely overcast, as measured in the Beaufort Sea in July 2011. **Figure 1** plots the normalized spectral incident irradiance for four distinct sky conditions: brilliantly clear (BC), partly cloudy with solar disk visible (PC-SDV), partly cloudy with solar disk barely visible (PC-SDBV), and completely overcast with solar disk not visible (CO-SDNV). The spectral composition of the incident irradiance changes as the cloud cover changes. Clouds absorb more light at longer wavelengths relative to shorter wavelengths, thus increasing the fraction of the incident irradiance contributed by shorter wavelengths. For example, the E(500 nm)/E(1600 nm) ratio is 7.6 for clear skies and 14.2 for completely overcast. When calculating the broadband transmittance, appropriately weighting the spectral transmittance with the spectral incident irradiance is important. The fraction of the entire solar incident irradiance spectrum contained in the 400–700 nm and 400–1000 nm wavelength regions are summarized in the insert to **Figure 1**. The fraction in the 400–1000 nm region ranges from 0.72 for BC conditions to 0.78 for CO-SDNV conditions. Observations made by the MOSAiC atmosphere program (Shupe et al., 2022) were used to determine which of the four sky conditions to use on a particular day. A single sky condition was used for each day.

The radiative transfer model uses spectral absorption coefficients and scattering coefficients to calculate transmittance. Absorption coefficients for pure, bubble-free ice are from laboratory (Grenfell and Perovich, 1984) and field studies (Warren and Brandt, 2008; Warren, 2019). Values for clear water are from Smith and Baker (1981). Scattering coefficients for different snow and ice types were derived from field observations of albedo and transmittance (Grenfell and Maykut, 1977; Light et al., 2008; 2015). Scattering is assumed to be isotropic in the model. Absorption coefficients for ice and water show a strong spectral dependence, increasing rapidly with wavelength. In contrast, scattering coefficients vary greatly between snow and ice types but are constant with wavelength because the scatterers—snow grains, air bubbles, brine pockets—are much larger than the wavelengths of solar radiation (Grenfell and Maykut, 1977). Scattering coefficients vary greatly between snow and ice types and evolve over the annual cycle (Grenfell and Maykut, 1977; Light et al., 2008; 2015).

Calculated spectral transmittances were combined with the incident spectral irradiance to compute the wavelength-integrated transmittance (T_B; Equation 1).

$$T_B = \frac{\sum_{i=400}^{1000} E_i(\lambda)\, T_i(\lambda)}{\sum_{ii=400}^{1000} E_i(\lambda)}. \tag{1}$$

Throughout this paper, we refer to the wavelength-integrated (400–1000 nm) transmittance as the broadband transmittance and use the subscript B to denote broadband. Note that T_B does not refer to the entire spectrum, only the portion from 400 nm to 1000 nm, but little solar radiation penetrates the ice cover outside this range.

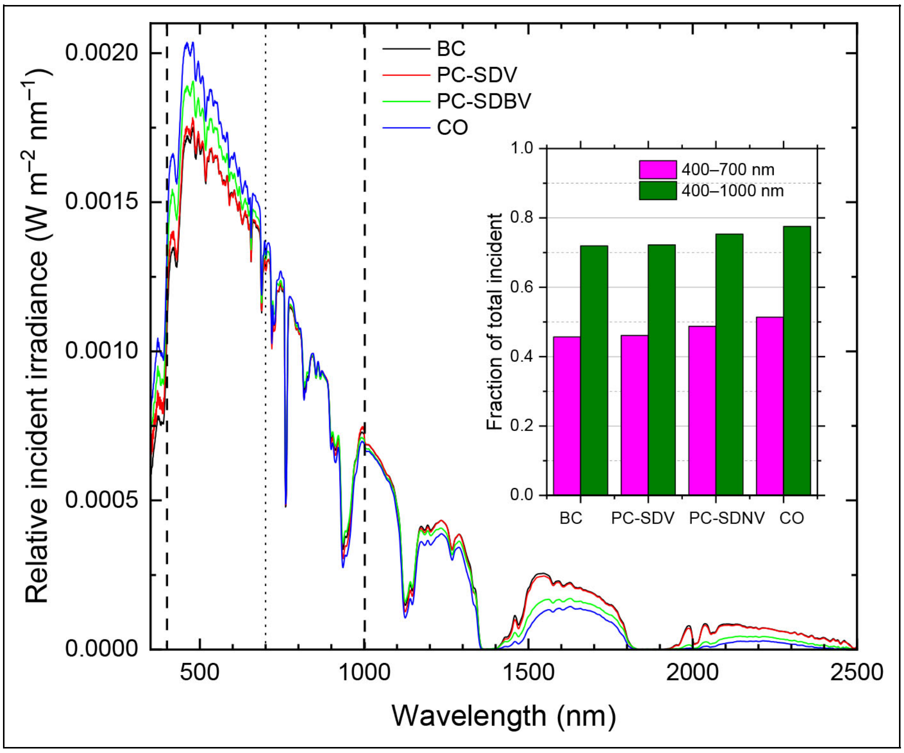

Figure 1. Observed incident solar irradiance under four sky states. Incident irradiance spectra under clear skies (BC), partly cloudy with solar disk visible (PC-SDV), partly cloudy with solar disk barely visible (PC-SDBV), and completely overcast with solar disk not visible (CO) based on observations made in the Beaufort Sea in 2011. The plotted irradiance is normalized so that the integral is equal to one. The inset bar chart shows the fraction of the total broadband irradiance contributed from 400 to 700 nm and from 400 to 1000 nm.

Physical properties of the ice cover are key input parameters to the model. During the MOSAiC field experiment (Nicolaus et al., 2022), there were repeated extensive transects characterizing the state of the ice cover (Itkin et al., 2023). These surveys were several kilometer-long loops with dimensions that changed occasionally due to ice deformation and repositioning the Central Observatory during the spring to summer transition. Each survey consisted of measurements at more than one thousand points along the transect with 1–5 m spatial sampling (Itkin et al., 2023). During winter and spring, snow depth (H_s) and ice thickness (H_i) were measured at each point. During summer, ice thickness was measured, along with the thickness of the surface scattering layer (H_{ss}; Smith et al., 2022) for bare ice, and the pond depth (H_p) for ponded ice (Webster et al., 2022).

Four cases were used to describe the surface state from these transects: cold snow, melting snow, bare ice, and ponded ice. Two or three layers were used in the model to define scattering coefficients for each condition. **Figure 2** summarizes the scattering coefficients for each layer in these four cases. Data from each point along the transect were used to define three layers with distinct scattering coefficients. The thickness of Layer 1 was measured directly during the transect as the snow depth, surface scattering layer thickness, or the pond depth. If snow or surface scattering layer surfaces were present (H_s), then the thickness of the second layer is the freeboard of the ice (F_f) calculated as

$$H_2 = F_f = \left(\frac{\rho_w - \rho_i}{\rho_w}\right) H_i - \rho_s H_s,$$

where ρ_w is the density of ocean water (1.02 g cm^{-3}), ρ_i is the density of ice (0.90 g cm^{-3}), and ρ_s is the density of the surface layer (snow or surface scattering = 0.33 g cm^{-3}). Applying the densities gives

$$H_2 = F_f = 0.1H_i - 0.33H_s. \tag{2}$$

The thickness of the third layer is simply $H_3 = H_i - H_2$. Ponded ice had two layers, a surface layer equal to the pond depth ($H_1 = H_p$) and a second layer with thickness equal to the ice thickness ($H_2 = H_i$).

Results

Transmittance time series at one point

The evolution of calculated transmittance at one specific location where continuous mass balance measurements were made provides an overview of the dominant features of the temporal change. Autonomous ice mass balance buoys were deployed during the MOSAiC field campaign (Nicolaus et al., 2022; Perovich et al., 2023). These buoys measured a time series of snow depth and ice thickness. **Figure 3a** shows snow depth and ice thickness from April through July for a buoy deployed in second year ice at MOSAiC station L2. This buoy was initially placed (October

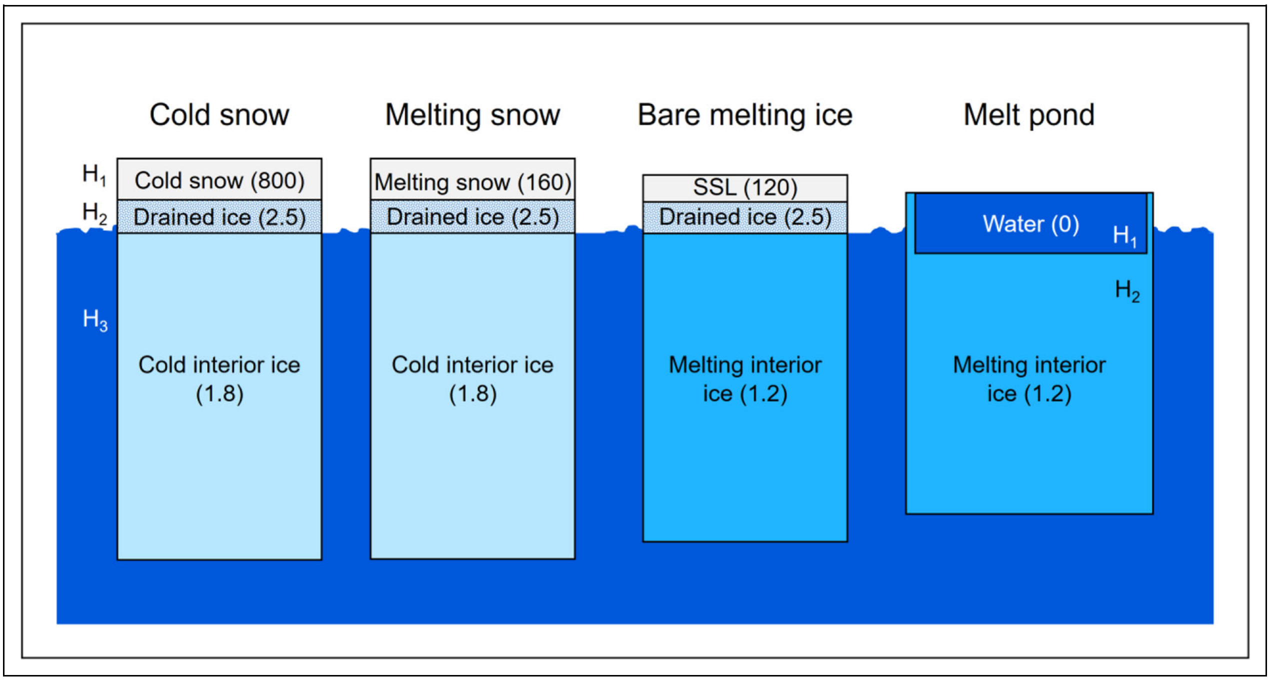

Figure 2. Layer type and scattering coefficients for the four ice states. Observation-based scattering coefficients (units of m^{-1}) are shown in parentheses. SSL denotes the surface scattering layer.

2019) 15 km southeast of the MOSAiC Central Observatory in the Distributed Network (Rabe et al., 2024). The maximum snow depth was 0.25 m in April 2020, and the maximum ice thickness was 1.90 m in May 2020. As the snow melted in June, the underlying bare ice was exposed on June 29, 2020. The final confirmed ice thickness was 1.29 m on July 11, 2020. After this time, a melt pond formed around the buoy and the buoy was no longer fixed in the ice. The reference frame was lost and the interpreting of the buoy data was ambiguous. The evolution of the ice showed four distinct phases: (1) cold dry snow, (2) melting snow, (3) transition from snow-covered ice to bare ice, and (4) thinning bare ice.

The snow depth and ice thickness data were used to define layers in the radiative transfer model as described in the Approach section. Once the snow cover completely melted, a surface scattering layer 0.03 m thick was used as the top layer. This value was selected based on transect observations (Webster et al., 2022; Itkin et al., 2023) and microstructure measurements (MacFarlane et al., 2023). **Figure 3b** shows the time series of spectral and broadband transmittance. During Phase 1, with cold snow-covered ice, transmittances were small. Broadband transmittances (T_B) were less than 0.001. The peak spectral transmittance was at 470 nm but was only about 0.002. Beyond 800 nm transmittances were negligible. Once the snow began to melt (Phase 2), there was a large increase in T_B to 0.008. Transmittance at 470 nm increased an order of magnitude to 0.02. At wavelengths greater than 800 nm, the relative increase was even larger, but the transmittance was still less than 10^{-5}. The remainder of Phase 2 had a small steady increase as the snow melted and thinned. There was another sharp jump in transmittance in Phase 3 as the surface became snow-free and T_B increased by about a factor of six to values around 0.07. Finally, in Phase 4, there was a steady increase in transmittance as melt thinned the ice. At the end of ice observation on July 21, 2020, T_B was 0.12, $T(470)$ was 0.17, and $T(700)$ was 0.11.

The computed results from transmittance time series are comparable to the observed evolutionary phases reported by Tao et al. (2024). They made autonomous measurements of spectral albedos and transmittances at three fixed locations. Having the time series from three stations with different sea ice and surface conditions resulted in their time series showing three phases: (1) dry snow, (2) melting snow and pond formation, and (3) advanced melt, as a melt ponding event was observed directly after the melt onset. Overall, the difference between studies is that we divided the Tao et al. (2024) phase 2 into two separate phases: snow melt and snow-free bare ice. In particular, their site LM, consisting of snow depth 0.18 m and ice thickness 1.59 m at the end of March, showed a more similar seasonal evolution to the four phases reported in this paper.

Transmittance along survey lines

Spectral and broadband transmittances, as well as transmitted photosynthetically active radiation (PAR), were estimated using ice transect data from May, June, and July. Results from May 7, 2020, representative of Phase 1, are presented in **Figure 4**. The top panel shows the surface type and the snow and ice thicknesses along the transect. Large variability in snow depth and ice thickness is evident. This physical variability is manifested in the computed broadband transmittance shown in the bottom panel, with broadband transmittance ranging from 10^{-5} to 0.014. Transmittances through this snow-covered ice

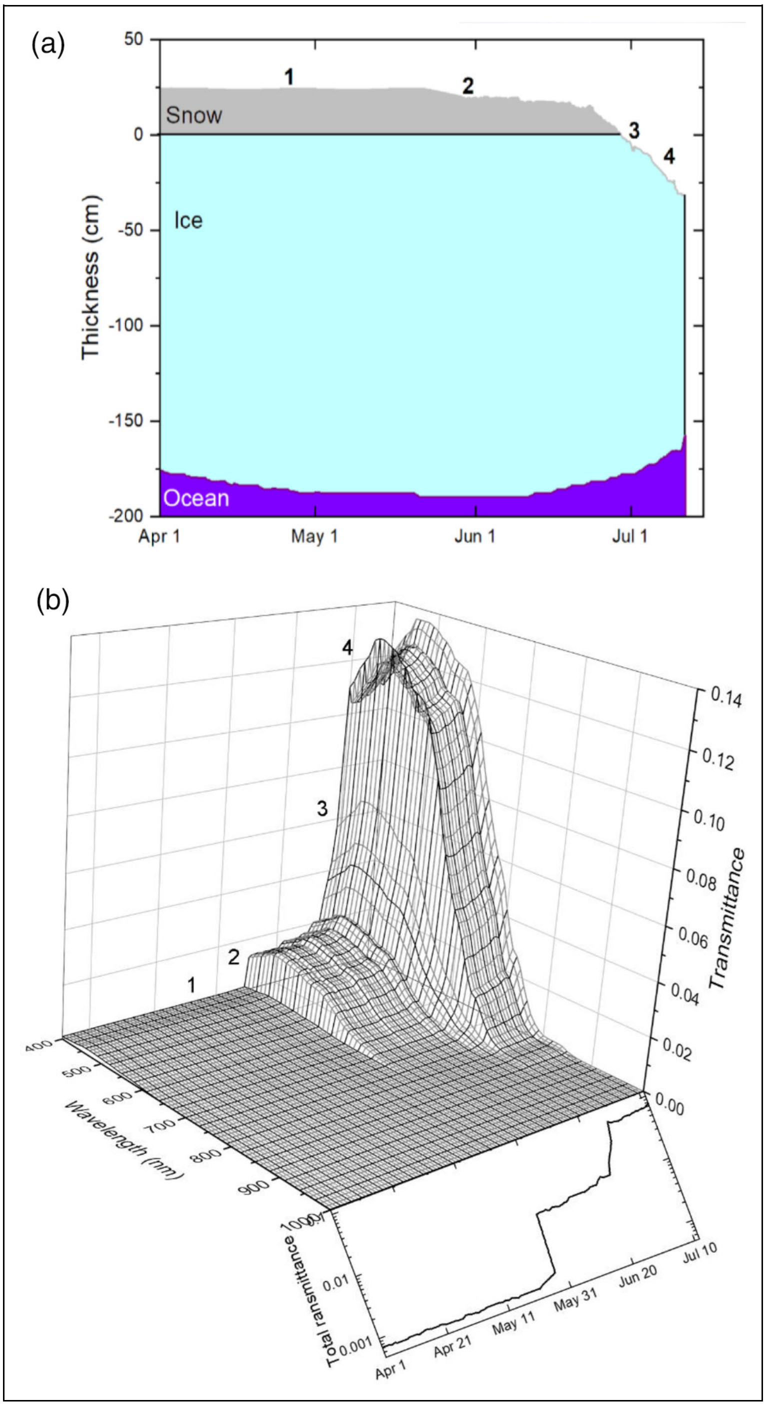

Figure 3. Mass balance and spectral transmittance at MOSAiC site L2 in 2020. (a) Time series of sea ice mass balance and (b) calculated estimates of spectral and broadband transmittance at site L2. The four numbers in each panel refer to the evolutionary cycle of (1) cold dry snow, (2) melting snow, (3) transition from snow-covered to bare ice, and (4) thinning of bare ice.

were small. The mean was 0.00082 and the median was 0.00037. The median is smaller than the mean because of the large contributions to the mean from points with thin snow and thin ice.

Figure 5 shows results from July 25, 2020, as the melt phase was nearing its seasonal peak. By this time, the snow cover was gone and the gray-shaded area in **Figure 5a** represents the surface scattering layer. The red areas are melt ponds. At first glance there are similarities between May 7 (**Figure 4**) and July 25 (**Figure 5**). Both express large variations in ice thickness and in transmittance. A closer look at **Figure 5b** shows a major difference. The y-axis is two orders of magnitude greater than in **Figure 4b**. The mean and median of the computed transmittance on July 25 were 0.096 and 0.053, respectively, ranging from 0.0055 to 0.76 over the transect. The smallest values on July 25 were similar to the largest values on May 7. The increase in transmittance is due to the removal of the snow cover, thinner ice, and the presence of melt ponds. The largest transmittances were through ponded ice.

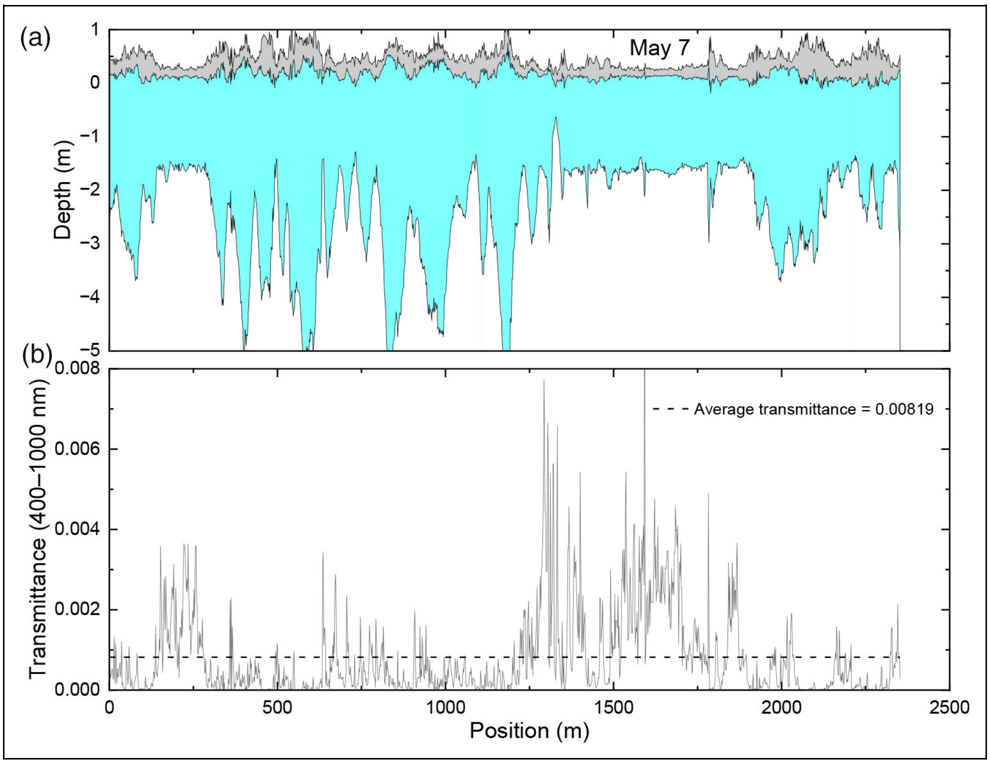

Figure 4. Ice profile and transmittance results from May 7, 2020 (late cold snow Phase 1). (a) The top panel shows snow depth (gray) and ice thickness (cyan) along the transect line. (b) The bottom panel shows the calculated transmittance along the transect line. The mean transmittance (black dashed line) was 0.00082, the median was 0.00037, and the range was from 3.4×10^{-7} to 0.014.

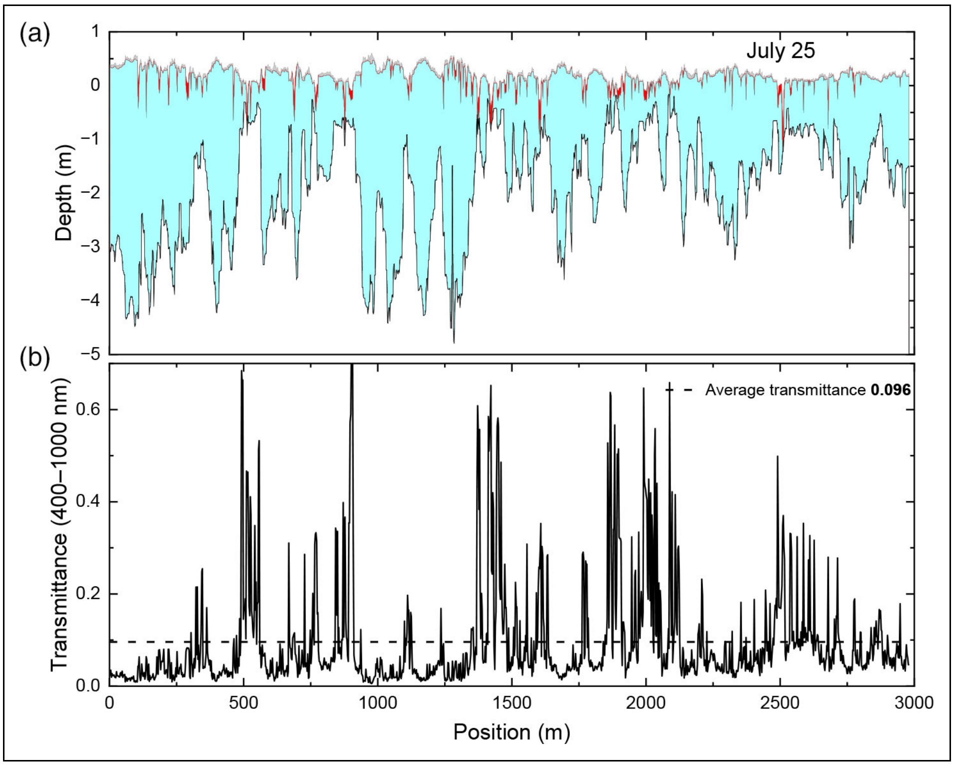

Figure 5. Ice profile and transmittance results from July 25, 2020 (thinning of ice Phase 4). (a) The top panel shows the surface scattering layer (gray), pond depth (red), and ice thickness (cyan) along the transect line. (b) The bottom panel shows the calculated transmittance along the transect line. The mean transmittance was 0.096, the median was 0.053, and the range was from 0.0055 to 0.76. Note that the y-axis scale is two orders of magnitude larger than in **Figure 4b**.

Results from May 7 and July 25 illustrate the extreme changes in transmittance between pre-melt and full melt conditions. In a closer look at the evolution of transmittance as the melt season progressed, using seven selected dates, changes in ice surface conditions are evident (photographs from May 7, June 29, July 5, July 10, July 13, July 20, and July 25 presented in **Figure 6**). On May 7 the ice was snow-covered. By June 29 most of the snow was gone and melt ponds had formed. As summer continued, the ice thinned, the ponds grew darker, the snow melted, and the melting ice formed a surface scattering layer. From June 29 to July 25 transect line results showed a general decrease in the mean surface scattering layer thickness (0.08 m to 0.05 m) and of the ice thickness (2.35 m to 2.07 m). These two factors resulted in a general increase in transmittance. The pond fraction was determined from the transect data. It increased from June 29 (0.09) to July 10 (0.20), reduced due to some pond drainage on July 20 (0.16), and then increased to July 25 (0.18; Webster et al., 2022).

Transmittances were calculated along transect lines on these 7 days and are presented on the right-hand side of **Figure 6**. In addition to box-and-whisker plots, showing the mean and median for each day, the transmittance at each point along a transect is plotted, with a log-normal probability density function of the

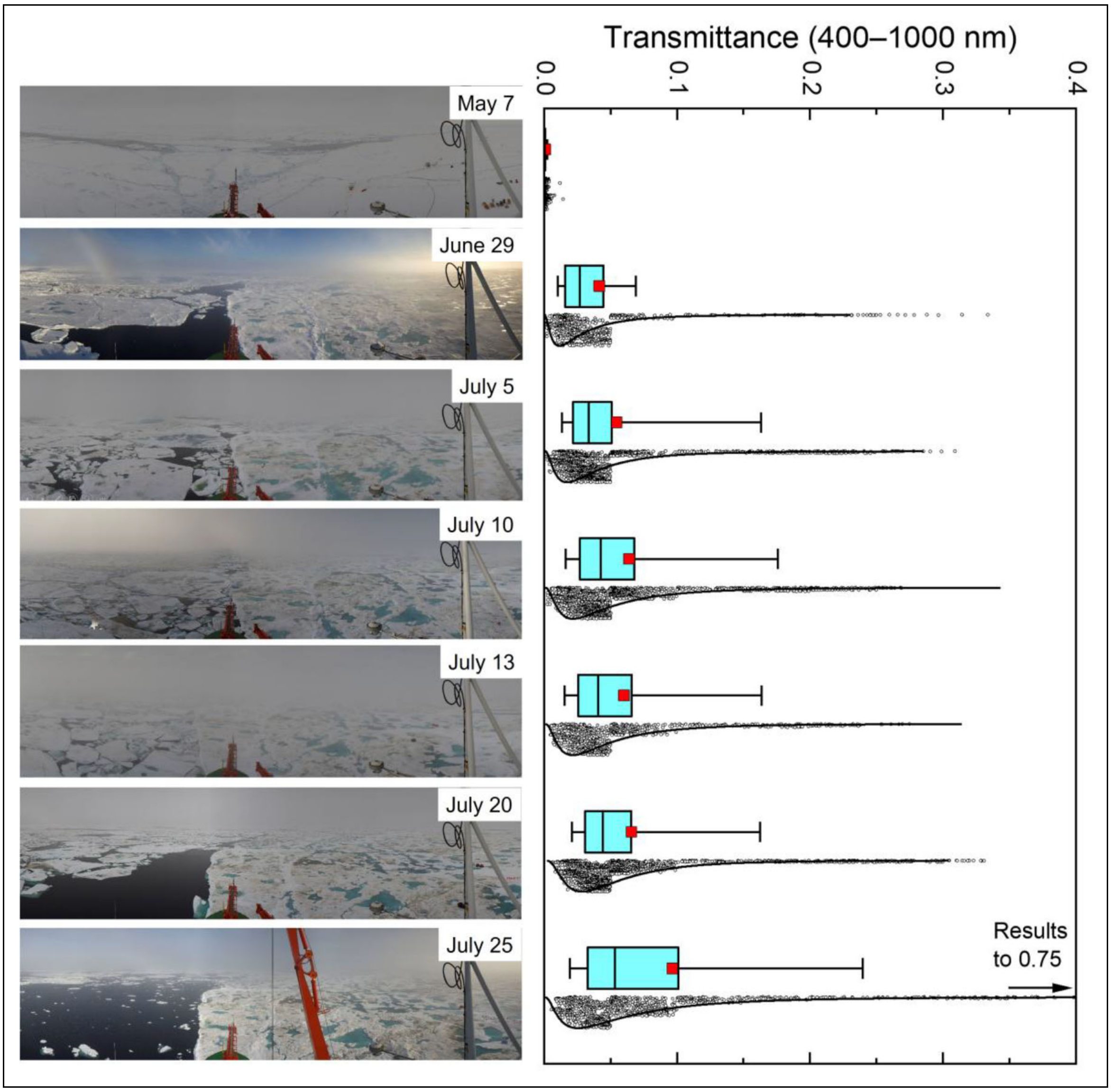

Figure 6. Time series of photographs and transmittance as the 2020 melt season progressed. Left side: Photographs of the ice cover, taken by a panorama camera (Panomax) positioned in the crow's nest of *Polarstern*, on 7 days in spring and summer when transmittance was calculated. The frame of view in all photos is toward the bow, with the Central Observatory, over which transect estimates were made, to the starboard (right side) of the image. Right side: Summary of transmittance results for transects on the same 7 days. These box-and-whisker plots show the mean (red square), the median (black vertical line in the cyan box), and the transmittance at each point along the transect (small symbols). The black curve along the individual transmittances is the log-normal probability density function distribution. The July 25, 2020, transmittance data extend (off panel) to a maximum value of 0.75.

individual transmittances. On each day, the individual transmittances show a cluster of points for transmittances less than 0.05, with a long tail of increasing transmittance. Variability in transmittance depends primarily on three factors: surface scattering layer depth, ice thickness, and, most importantly, whether the surface is bare or ponded. Melt ponds are the source of the long tail of transmittances. By July 25, 2020, there were more bare ice transmittances in the 0.05 to 0.10 range and pond transmittances as large as 0.75 due to the overall thinning of the ice. The mean transmittance was always greater than the median due to the large transmittance from the ponds. The median was determined by the large number of bare ice cases, while the mean was heavily influenced by the large transmittance from the relatively few melt ponds.

Light transmission through melt ponds has long been observed to be larger than through bare ice (Grenfell and Maykut, 1977; Light et al., 2008; Frey et al., 2011; Light et al., 2015). **Figure 7** shows the average broadband transmittance through bare ice and through ponded ice for 6 summer days analyzed in this paper. The average pond transmittances are 4–6 times larger than the average bare ice transmittances. Ponds transmitted more light than bare ice but typically had a smaller area fraction (*A*). The total area-averaged broadband transmittance from bare ice and ponded ice is

$$T_{bTotal} = A_i \underline{T_{bi}} + A_p \underline{T_{bp}}, \tag{3}$$

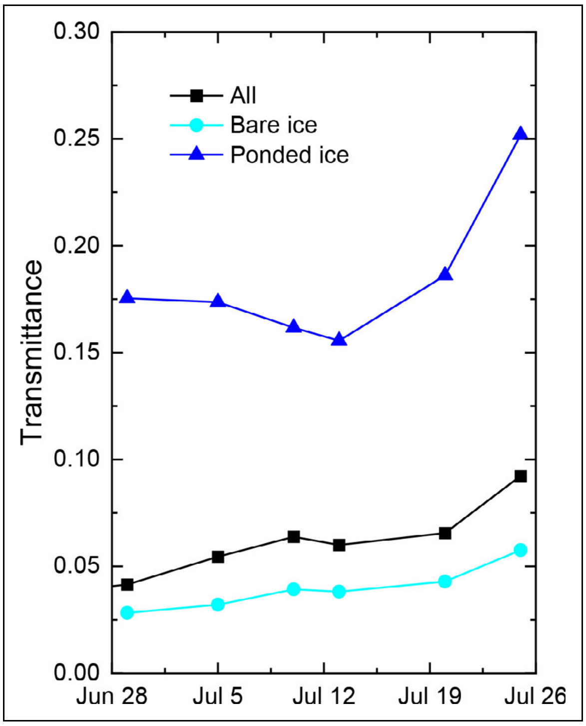

Figure 7. Time series of average transmittance through bare ice and ponded ice during the 2020 melt season. Total average transmittance is shown, as well as averages for bare and ponded ice, for transects on 6 summer days during the melt season.

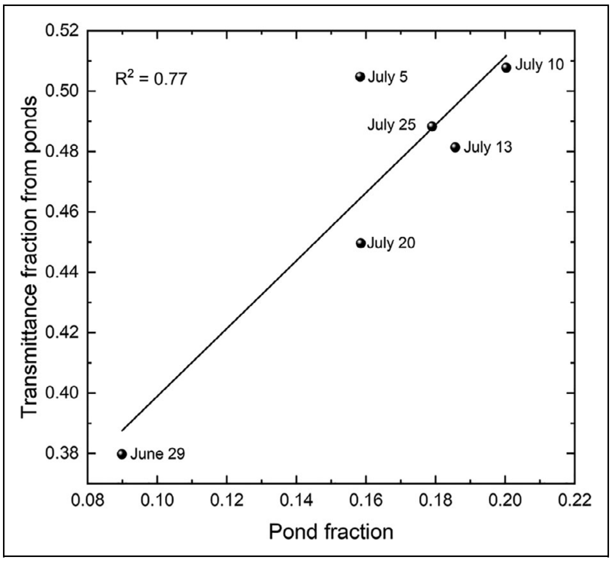

Figure 8. Transmittance contribution from melt ponds versus fraction of melt ponds in 2020. Contribution of melt ponds to total transmittance versus coverage by melt ponds for transects on 6 summer days. Black line represents linear regression analysis.

where the bars represent average broadband values for ice (*bi*) and ponds (*bp*). For much of July ponds contributed roughly half of the total transmittance even though they covered only 16–20% of the total ice area (**Figure 8**).

Discussion

Upper ocean heating through ice and leads

The Results section provides calculated estimates of transmittance, based on observed properties of the ice/snow column at the MOSAiC Central Observatory examined for variability over space and time. These transmittances can be combined with observed incident irradiances to compute the amount of solar energy that passed through the ice into the upper ocean. First, we used the mass balance data from the L2 buoy to determine a time series of transmitted solar energy at a single point.

During MOSAiC, the atmosphere team made extensive measurements of the broadband incident irradiance (I_b) using pyranometers, as well as observations of cloud conditions (Shupe et al., 2022; Cox et al., 2023). The incident irradiance measurements covered the entire solar spectrum, while the computed transmittances only included 400–1000 nm. Because of absorption in the ice cover, negligible sunlight beyond 1000 nm was transmitted through the ice into the upper ocean. The amount of solar energy deposited through the ice to the upper ocean (Q_o) over a time interval (Δt) is

$$Q_o = E_b E^* T_b \Delta t, \tag{4}$$

where E^* is the fraction of the total incident irradiance contained in the 400–1000 nm band. The insert in **Figure 1** summarizes the values of E^* used for the four sky conditions.

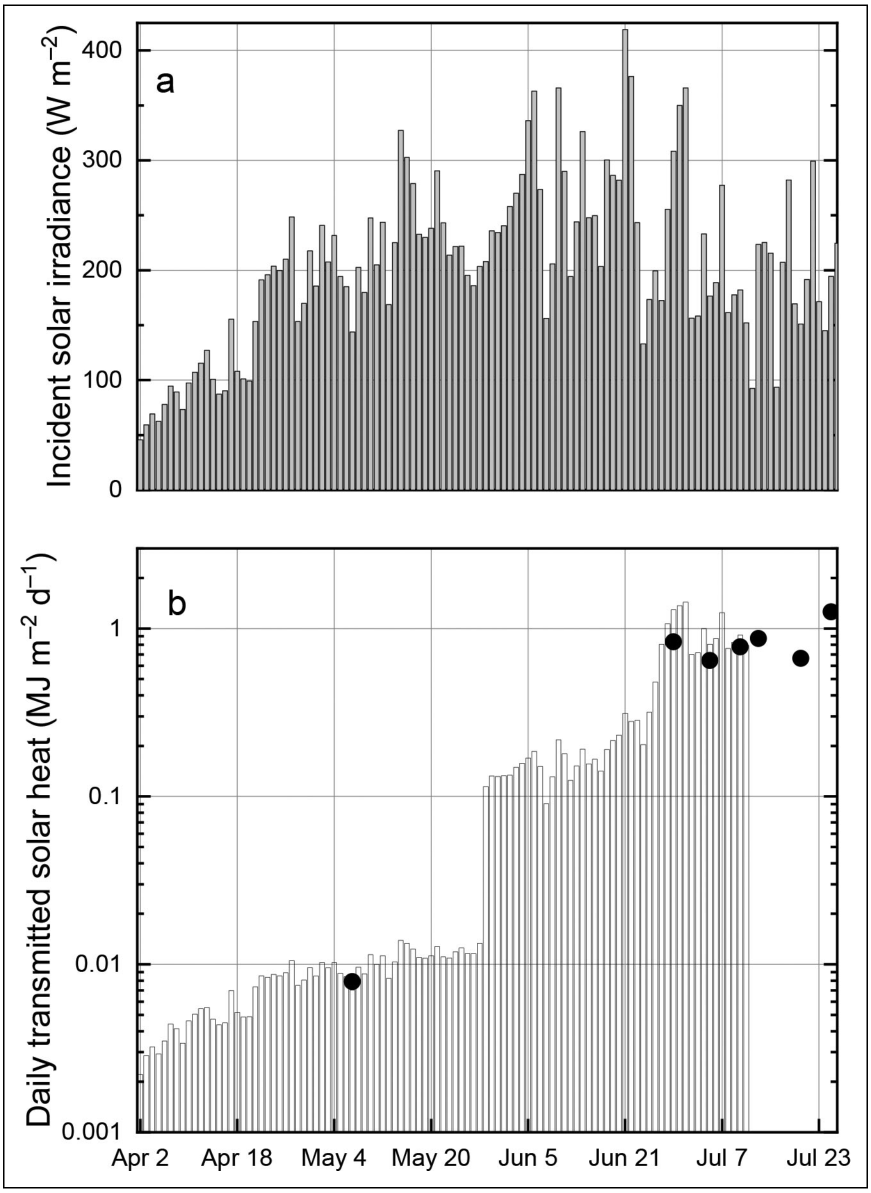

Figure 9. Observed daily incident irradiance and calculated transmitted solar heat for April–July, 2020. (a) Daily broadband incident shortwave irradiance from 300 to 3600 nm measured at MOSAiC station L2. (b) Daily solar energy transmitted through the ice at the L2 ice mass balance buoy (bars), with the average transmitted solar energy along the transect line on the days plotted (black circles). Note log-scale vertical axis.

The daily incident shortwave irradiance for April–July is plotted in **Figure 9a**. The seasonal cycle of incident irradiance is evident in the plot, with the largest monthly average incident irradiance of 267 W m^{-2} in June and the smallest (125 W m^{-2}) in April. There are day-to-day fluctuations up to a factor of 2.5 resulting from variations in cloud cover. Daily values of transmitted solar energy calculated at the L2 station are plotted in **Figure 9b**. The large jump in transmitted solar heat at the end of May was due to the shift to a melting, thinning snow cover. This onset of melt was observed from the radiometric suite of measurements to have occurred on May 26. The L2 station was bare ice until mid-July. The shape of the transmitted solar energy curve in **Figure 9** is similar to the calculated transmittance curve in **Figure 3** showing the same four phases. There are more fluctuations in the solar energy curve due to the daily variability in the solar incident irradiance on sunny days and cloudy days. The total heat input through the ice to the upper ocean for this time period was 20 MJ m^{-2}, roughly equivalent to 0.07 m of ice melt per meter squared. The observed bottom melt at the L2 buoy was 0.30 m, indicating that there were likely additional sources of ocean heat. These sources include light transmitted through leads and melt ponds, as well as encountering warmer waters in Fram Strait. Different locations might produce different total amounts of transmitted solar heat, as was found by Ran et al. (2024), but the trends would remain the same.

Transmittances from transect data were used to examine the spatial variability of transmitted solar energy at a specific time. This variability included variations in snow depth, pond depth, and ice thickness and contributions from ponded and bare ice. The black circles in **Figure 9b** represent the spatial average across the transect for that day, giving a broader perspective than the single point bare ice results from the L2 station (bars in **Figure 9b**). Differences in transect-average and L2 transmitted solar energy values range from -13% to 16%. The greatest difference of 16% was on July 10 when the transect pond fraction was large (0.2) and the transect transmission was greater.

Light transmission through leads also contributes to solar heating of the upper ocean. This contribution can be large due to the small albedo of leads and the fact that any light not reflected is directly deposited into the ocean. The total amount of shortwave radiation reaching the upper ocean (Q_T) is a combination of transmission through the ice and through leads, each weighted appropriately by the ice concentration (C). Formally this amount is

$$Q_T = E_b E^* T_b \Delta t C + (1 - \alpha_l)\Delta t(1 - C)E_b E^*,$$

where α_l is the lead albedo ($\alpha_l = 0.07$; Pegau and Paulson, 2001).

Ice concentrations were obtained from the NOAA/NSIDC Sea Ice Concentration Climate Data Record (Meier et al., 2017). The time series of ice concentration on the grid cell following the MOSAiC drift is plotted in **Figure 10a**. Ice concentration was high throughout the entire period. The ice concentration was equal to 1.00 during 73% of the time, and the minimum value was 0.93, suggesting a maximum open water lead fraction of only 0.07. This small fraction limited the contribution of leads to the solar energy input to the ocean. Accumulated transmitted solar energy through the ice, into the leads, and the combined total are plotted in **Figure 10b**, where ice results are from the L2 buoy calculations presented in **Figure 9**. Until the beginning of June, solar energy input at MOSAiC was dominated by the contributions from leads. Very little light penetrated through the ice due to the presence of snow. On May 7, the average transmittance through bare ice was only 0.00082 compared to 0.93 for leads. Lead transmittance was three orders of magnitude greater. Even if the lead fraction was only 0.01, the contribution from leads was still an order of magnitude greater than that from snow-covered ice.

Starting in early June, the snow cover melted, ponds began to form, and transmission through the ice increased. By July, the contribution from transmission through the ice exceeded that of leads. In summer, transmission through leads was still important, but the contributions from the ice were generally greater due to the much greater ice area fraction. On July 25, the average transmittance through bare ice was 0.06 and through melt ponds was 0.26. Thus, leads transmitted 15.5 times as much light as bare ice and 3.6 times as much as ponds per unit area. On this day, the surface was 3% leads, 75% bare ice, and 22% melt ponds. Leads contributed 22% of the transmitted sunlight, ponds 44%, and bare ice 34%, showing that ponds were the dominant contributor on this day. Larger lead fractions are common in summer and would increase the contribution from leads. For example, if the July 25 lead fraction was 0.06, the total lead contribution would be the same amount as ponds. The total accumulated solar energy transmitted to the upper ocean through July 11 was 34 MJ m^{-2}. How this heat was partitioned between lateral melting, bottom melting, and storage in the ocean is not known. However, that amount of heat could potentially melt 0.11 m of ice per square meter. Overall, including leads in our analysis increases the solar heat input to the ocean by about 60%.

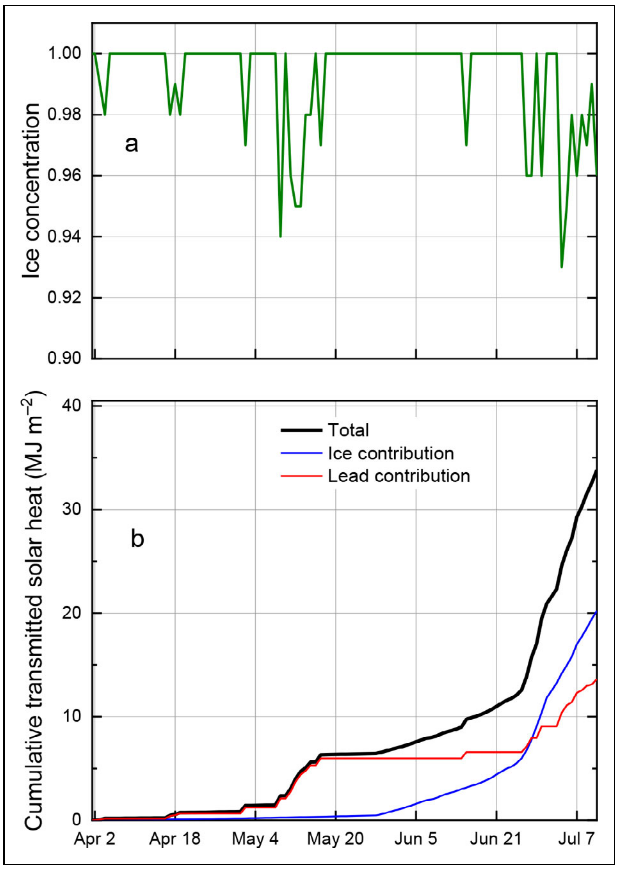

Figure 10. Ice concentration and transmitted solar energy for April–July, 2020. (a) Daily ice concentration at the MOSAiC Central Observatory obtained from the NOAA/NSIDC Sea Ice Concentration Climate Data Record (Meier et al., 2017). (b) The cumulative solar energy transmitted to the upper ocean through the ice, through leads, and the combined total. The ice contribution was determined using data from the L2 ice mass balance buoy (**Figure 9**).

Determining ice concentration in summer using passive microwave is complicated due to the presence of meltwater. As the July 25 results demonstrate, leads contribute much more solar heat to the ocean than bare ice or ponded ice. Uncertainty in the ice concentration can have a significant effect on the amount of solar heat deposited in the ocean.

Comparison to fewer points

Having such extensive in situ observations of ice, snow, and pond properties as those obtained during MOSAiC is rare. This dataset allowed a detailed examination of the spatial variability of transmittance versus representative

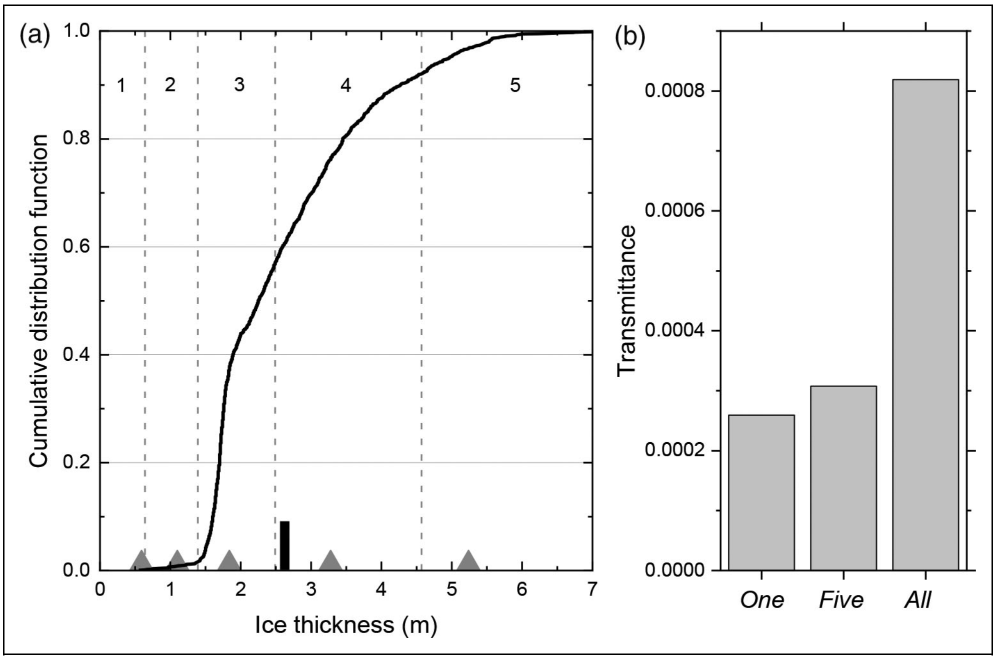

Figure 11. Model comparison of transmittance on May 7, 2020. (a) Cumulative distribution of ice thickness from thickness measurements made on May 7. Vertical dashed lines denote the five thickness categories in the CICE model. Triangles show the observed average thickness in each category. The black bar is the observed average ice thickness of the entire distribution used in the *One* case calculation. (b) Average transmittance calculated using one point (*One*), five points (*Five*), and all the data points (*ALL*).

spatially averaged values, which affords the opportunity to carry out analyses of the sensitivity of results to data density and coarseness. In this section we use results from May 7 and July 25 to compare the average transmittance determined with the full suite of physical properties (*All*) to two additional scenarios that use more limited descriptions of the snow and ice conditions. The first scenario uses only a single average ice thickness and snow depth for May 7, a pond fraction and a single average pond depth for July 25, and average ice thicknesses for ponded and bare ice (*One*). The other case uses the five-category ice thickness distribution (*Five*) used in the Los Alamos sea ice model CICE (Hunke et al., 2015). This distribution is also used in the Community Earth System Model 2 (Danabasoglu et al., 2020). The treatment uses average values for five thickness categories, with thickness ranges of (1) 0.00–0.64 m, (2) 0.64–1.39 m, (3) 1.39–2.47 m, (4) 2.47–4.57 m, and (5) 4.57 and greater. Each category may include a mix of snow-covered ice, bare ice, and ponded ice with appropriate areal fractions. We used transect observations to provide area fractions and average snow, ice, and pond thicknesses for each of the five thickness categories. These results were then used in the two-stream radiative transfer model.

The cumulative ice thickness distribution for May 7 is shown in **Figure 11a**. For the *One* case, the average snow depth of 0.32 m and ice thickness of 2.61 m were used to compute the transmittance. For the *Five* case, the average observed snow depth and ice thickness were calculated for each of the five thickness categories. The transmittance for each category was then computed using these values and weighted by the fractional area of each category to get the overall average. Conditions on May 7 were cold, snow-covered ice, and transmittances were small in all three cases. However, the average transmittances from *One* and *Five* are less than half of *All* (**Figure 11b**). In this snow-covered situation, a few sites with relatively thin snow and ice make an outsized contribution to the transmittance in the *All* case that is missed in the *One* and *Five* cases due to the use of a single average snow depth for each category

Results for the melt season case of July 25 are shown in **Figure 12**. The ice cover was a mix of bare ice (82%) and melt ponds (18%). The *One* case had two components: bare ice with a 0.045 m surface scattering layer and 2.01 m of melting ice, along with a ponded area with a depth of 0.18 m over 1.64 m of melting ice (**Figure 12a**). The *Five* transmittance calculation had ten components, five for bare ice and five for ponded ice. The bare ice components had surface scattering layer thicknesses determined from observations. Transmittances on July 25 for *One* and *Five* were smaller than *All*, with values of 0.064 for *One*, 0.084 for *Five*, and 0.092 for *All*. The contribution from ponds to transmittance was approximately 50% in all three cases.

The percent differences were smaller on July 25 than on May 7 due in part to considering both bare and ponded ice. In general, *One* and *Five* transmittances will always be smaller than *All*. This effect is because we used a linear process to determine average values for the physical properties and then used those values in an exponential function determining transmittance, an example of Jensen's Inequality (Jensen, 1906). The more points that are considered, the better the agreement with the *All* cases.

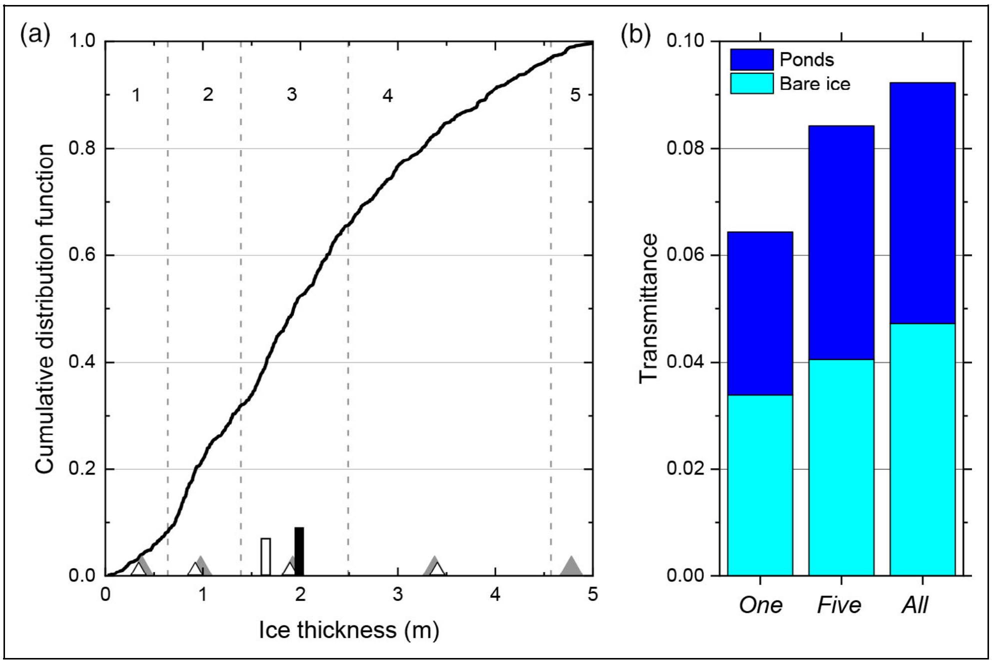

Figure 12. Model comparison of transmittance on July 25, 2020. (a) Cumulative distribution of ice thickness from a thickness transect made on July 25. Vertical dashed lines denote the five thickness categories in the CICE model. The black bar is the observed average ice thickness of the bare ice; the white bar, the average thickness of the ponded ice. The gray triangles are the average thickness of bare ice in each category; the white triangles, the average thickness of ponded ice. (b) Average transmittance calculated including bare ice and ponds using one point (*One*), five categories (*Five*), and all the data points (*ALL*).

We can provide context regarding the importance of these differences by calculating transmitted solar flux for the three cases on May 7 and July 25 (**Table 1**). On May 7, the transmitted solar fluxes are all only hundredths of a W m^{-2}; thus, differences between *All* and *One* and *Five* transmittances are all also very small. These differences are not significant from a heat perspective, though there may be implications for primary productivity. The transmitted solar flux on July 25 was 13.9 W m^{-2} for *All*, a significant amount of heat. The difference between *All* and *Five* is 1.2 W m^{-2}, which may be comparable to other uncertainties in energy balance calculations. The difference between *All* and *One* is 4.2 W m^{-2}, a significant difference for most considerations.

Photosynthetically active radiation

Primary productivity in the ice and upper ocean is determined in part by the amount of PAR. PAR is measured in units of photon flux density (µmoles of photons m^{-2} s^{-1}), distinct from the measurement of irradiance (energy per unit time over a specified area; W m^{-2}). Transmitted PAR ($T_{PAR}(\lambda)$) is calculated by converting transmitted irradiance ($T_{IRR}(\lambda)$) to transmitted photon flux density at individual wavelengths and then summing over the interval 400–700 nm using the relationship

$$T_{PAR}(\lambda) = \sum_{400}^{700} \frac{\lambda(T_{IRR}(\lambda))}{(nhc)} \Delta\lambda,$$

where n is Avogadro's number (6.025 × 10^{23}), h is Planck's constant (6.625 × 10^{-34} J s), and c is the speed of light (3 × 10^{17} nm s^{-1}). The total transmitted PAR (T_{PAR}) is the sum of $T_{PAR}(\lambda)$ from 400 nm to 700 nm.

The spatial distribution of T_{PAR} along the transect line was calculated for the snow-covered ice of May 7, 2020, and the ponded ice of July 25, 2020 (**Figure 13**). The T_{PAR} calculations do not include any representation of biota in the ice. There is tremendous spatial variability along the transect with T_{PAR} varying by three orders of magnitude on May 7 due to variations in snow depth and ice thickness. On July 25, T_{PAR} varied by two orders of magnitude due primarily to whether the surface was bare, melting ice, or

Table 1. Estimates of daily solar energy deposited in the upper ocean for three representations of transmittance

Case	E_r[a]	E_r 400–1000 nm	Transmittance	Transmitted flux (W m^{-2})
May 7, 2020				
One	144	0.775	0.000259	0.0289
Five	144	0.775	0.000308	0.0343
All	144	0.775	0.000819	0.0912
July 25, 2020				
One	194	0.775	0.0643	9.69
Five	194	0.775	0.0842	12.69
All	194	0.775	0.0923	13.92

[a] E_r is the incident solar irradiance (W m^{-2}).

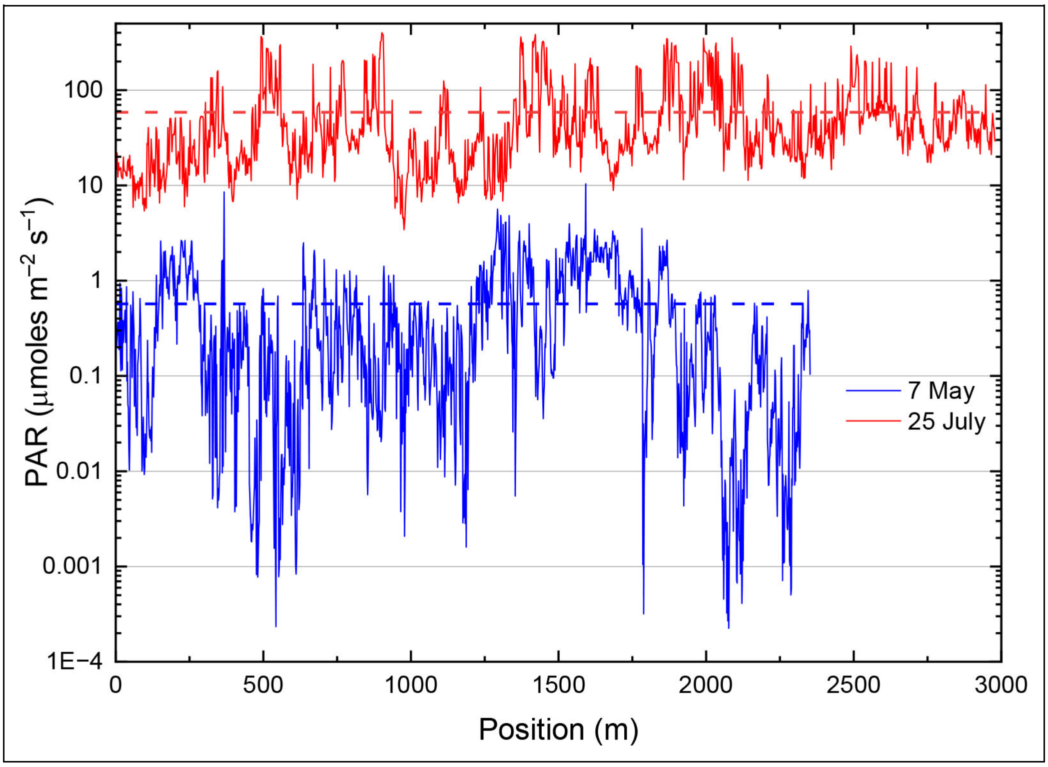

Figure 13. Transmitted PAR along the May 7 and July 25 transect lines in 2020. The dashed lines are the average values of photosynthetically active radiation (PAR) over the transect for that day.

Table 2. Summary statistics for transmitted photosynthetically active radiation (T_{PAR}), calculated using observed physical properties along the May 7 and July 25 transect lines in 2020

Parameter[a]	May 7	July 25
Mean	0.57	58.6
Median	0.24	33.8
Standard deviation	0.83	67.9
Minimum	0.00023	3.4
Maximum	10.4	401
Count	1486	1266

[a] Units are μmoles of photons m^{-2} s^{-1}; count is the number of points where T_{PAR} was calculated.

a melt pond. Mean values of T_{PAR} were two orders of magnitude larger on July 25 compared to May 7. T_{PAR} statistics for the two days are summarized in **Table 2**.

The probability distribution of T_{PAR} determined from the transect results is informative to know. It can be determined using a cumulative distribution function (CDF) of T_{PAR}. All values of T_{PAR} for a day were sorted smallest to largest, and then the CDF was calculated. **Figure 14** shows computed CDF for May 7 and July 25. As **Figure 14** illustrates, there is little overlap between May 7 and July 25, with only 1% of the May 7 points as large as the smallest July 25 values. **Figure 14** results can be used to determine what fraction of the transect had T_{PAR} values above a given threshold or within a particular range, providing insight for potential primary productivity.

Uncertainty

This work has focused on calculating estimates of transmittance at many points over transects kilometers long to explore the spatial variability, areal averages, and temporal evolution of transmittance. Two main sources of uncertainty enter into the calculations: the physical properties and the optical properties. The Magnaprobe measurements of snow depth, surface scattering layer thickness, and melt pond depth have an uncertainty of 0.01 m (Itkin et al., 2023). The uncertainty of ice thickness is about 0.1 m. These uncertainties will result in variability in the computed transmittance at an individual point. However, the uncertainties in physical properties are not systematic, so the impact on the statistics of more than 1000 measurements from each transect will be minor. Unconsolidated ridges are composed of a mixture of ice blocks and water resulting in a physically complex light field and uncertainty in transmittance.

The second source of uncertainty is in the absorption and scattering coefficients. Absorption coefficients for pure, bubble-free ice are well established (Warren, 2019). We did not include any sediments or ice algae in our analysis, as we had no information regarding them along the transect lines. Their presence would increase absorption and reduce transmittance. The calculated transmittances represent a maximum value assuming no sediments or algae. There is some uncertainty associated with the selection of the scattering coefficients. Light et al. (2008; 2015) established that there is a range of possible

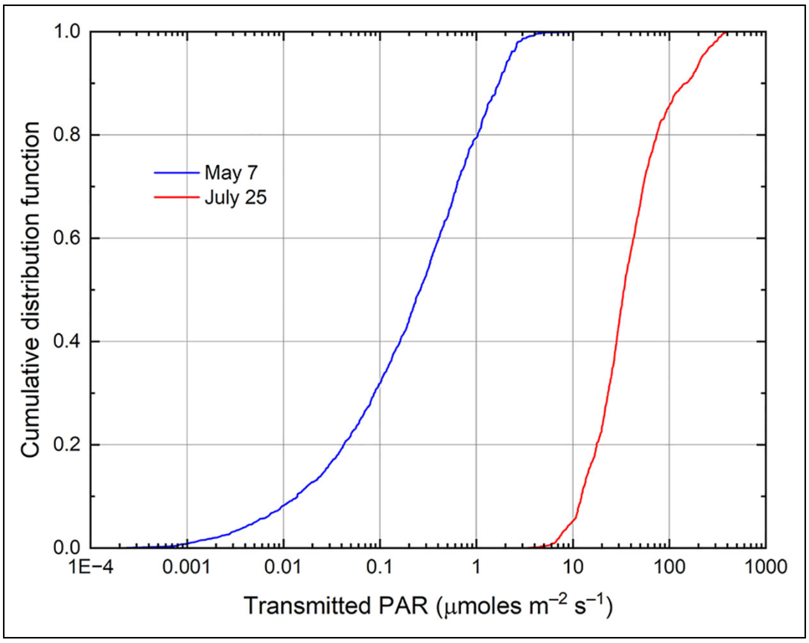

Figure 14. Cumulative distribution of transmitted PAR for the May 7 and July 25 transects in 2020. Cumulative distribution functions for transmitted photosynthetically active radiation (PAR) calculated using transect data from May 7 and July 25.

values of scattering coefficients for different snow and ice types. We selected values in that range consistent with analyses done in the past (Perovich, 2005).

Conclusions

The transmittance through the ice to the upper ocean at MOSAiC increased by two orders of magnitude over the time period from cold, snow-covered ice in May to thinner, melting ice in July. There were four distinct phases to this evolutionary cycle: (1) cold dry snow, (2) melting snow, (3) transition from snow-covered to bare ice, and (4) thinning of bare ice. Transmittance was much larger in the visible than in the near infrared.

Transmittances calculated using physical property observations made along transect lines showed large spatial variability. In spring, over spatial scales of tens of meters, transmittance varied by five orders. These variations were due primarily to differences in snow depth and ice thickness. Before melt took place, snow-free undeformed ice had the largest transmittance, while ridges with deep snow drifts had the smallest. During summer melt, transmittances varied spatially by two orders of magnitude due mainly to differences between ponded ice and bare ice, with a contribution from ice thickness variations. In summer, ponds had a major impact on the light field under the ice, transmitting on average 4–6 times as much light as bare ice. In late July, ponds covered about 20% of the ice surface and contributed 50% of the light transmitted through the ice into the upper ocean.

At the L2 site from July 1 to July 11, an average of 1.2 MJ m^{-2} d^{-1} were transmitted through the ice to the upper ocean. From April 1 through July 11, 20 MJ m^{-2} of solar energy was transmitted through the ice into the upper ocean. Including sunlight transmitted through leads increased the total solar input to the upper ocean to 34 MJ m^{-2}. The accumulated solar energy would likely have continued to increase through the remainder of July and into August. A next step for this work would be to explore the fate of the transmitted light. If ice algae are present in the skeletal layer of the ice, they could absorb some of the light and energy. Phytoplankton and particles in the water could also absorb transmitted light. How the light is attenuated with depth has repercussions for the partitioning of this light between bottom melt and storage of solar heat in the ocean.

Representing the detailed distribution of ice physical properties with only a few average values will always result in transmittance estimates that are smaller than those calculated using a full distribution of points. In spring, when the ice is snow-covered, so little light is transmitted that this underestimation is insignificant from a solar heat flux perspective. Summer solar energy transmission using the CICE sea ice model approach, with five thickness categories and three surface types, showed good agreement with the average value calculated using all the data points, differing by only 1.2 W m^{-2} and thus supporting the sufficiency of such a modeling approach.

Data accessibility statement

The L2 buoy data used in this paper are archived at the Arctic Data Center. The doi for this archived dataset is: https://doi.org/10.18739/A20Z70Z01. Data from the transects are all archived at the PANGAEA Data Publisher: https://doi.org/10.1594/PANGAEA.937781. Broadband solar irradiance measurements are available from https://doi.org/10.18739/A2PV6B83F. Photographs in **Figure 6** are available from https://doi.pangaea.de/10.1594/PANGAEA.938534.

Acknowledgments

Data used in this manuscript were produced as part of the international Multidisciplinary Drifting Observatory for the Study of the Arctic Climate (MOSAiC) with the tag MOSAiC20192020 and the Project_ID: AWI_PS122_00. We thank all people involved in the expedition of the Research Vessel *Polarstern* during MOSAiC in 2019–2020 as listed in Nixdorf et al. (2021).

Funding

DP, IAR, DC-S, and CP were supported by the NSF OPP-1724540, NSF OPP-1724424, and NSF OPP-2034919. MMS and BL were supported by NSF OPP-2138787. MW was supported by NSF OPP-2325430. CJC, MDS, and DC-S received support from NOAA's Global Ocean Monitoring and Observing Program through the Arctic Research Program (FundRef https://doi.org/10.13039/100018302) and the NOAA Physical Sciences Laboratory. MDS received additional support from NSF OPP-1724551. MMH and DC-S were supported by NSF OPP-2138788. ARM was supported by the Swiss National Science Foundation, project number P500PN_217845, and WSL Institute for Snow and Avalanche Research SLF, project number WSL_201812N1678. JS was supported by NASA Grant #80NSSC20K1121 and Horizon 2020 CRiceS #101003826. Additional funding was provided by the Canada 150 Research Chairs program, C150 Grant 50296, NO and FL were supported by the German Federal Ministry for Economic Affairs and Energy (BMWi) project ArcticSense (50EE1917A). RT and MN were supported by "Deutsche Forschungsgemeinschaft (DFG, German Research Foundation)—Project-ID 268020496—through the Transregional Collaborative Research Centre TRR-172 "ArctiC Amplification: Climate Relevant Atmospheric and SurfaCe Processes, and Feedback Mechanisms (AC)3."

Competing interests

The authors declare that they have no conflict of interest.

Author contributions

DP, BL, MS, MW, MH, DCS, IAR, and CP contributed to the conception and design of this work. MDS, MW, DC-S, IAR, CJC, PI, FL, ARM, MN, NO, MDS, and RT contributed to the acquisition of data. DP led the modeling work. All authors contributed to the analysis. All authors contributed to the drafting and revising of the manuscript. All authors have approved the submission of this manuscript.

References

Briegleb, BP, **Light, B.** 2007. A Delta-Eddington multiple scattering parameterization for solar radiation in the sea ice component of the community of the Climate System Model. NCAR/TN-472+STR. 100. DOI: https://doi.org/10.5065/D6B27S71.

Calmer, R, **de Boer, G**, **Hamilton, J**, **Lawrence, D**, **Webster, MA**, **Wright, N**, **Shupe, MD**, **Cox, CJ**, **Cassano, JJ.** 2023. Relationships between summertime surface albedo and melt pond fraction in the central Arctic Ocean: The aggregate scale of albedo obtained on the MOSAiC floe. *Elementa: Science of the Anthropocene* **11**(1): 00001. DOI: https://doi.org/10.1525/elementa.2023.00001.

Cox, CJ, **Gallagher, MR**, **Shupe, MD**, **Persson, POG**, **Solomon, A**, **Fairall, CW**, **Ayers, T**, **Blomquist, B**, **Brooks, IM**, **Costa, D**, **Grachev, A**, **Gottas, D**, **Hutchings, JK**, **Kutchenreiter, MC**, **Leach, J**, **Morris, SM**, **Morris, V**, **Osborn, J**, **Pezoa, S**, **Preußer, A**, **Riihimaki, LD**, **Uttal, T.** 2023. Continuous observations of the surface energy budget and meteorology over Arctic sea ice during MOSAiC. *Scientific Data* **10**: 519. DOI: https://doi.org/10.1038/s41597-023-02415-5.

Danabasoglu, G, **Lamarque, JF**, **Bachmeister, J**, **Bailey, DA**, **DuVivier, AK**, **Edwards, J**, **Emmons, LK**, **Fasullo, J**, **Garcia, R**, **Gettelman, A**, **Hannay, C**, **Holland, MM**, **Large, WG**, **Lauritzen, PH**, **Lawrence, DM**, **Lenaerts, JTM**, **Lindsay, K**, **Lipscomb, WH**, **Mills, MJ**, **Neale, R**, **Oleson, KW**, **Otto-Bliesner, B**, **Phillips, AS**, **Sacks, W**, **Tilmes, S**, **van Kampenhout, L**, **Vertenstein, M**, **Bertini, A**, **Dennis, J**, **Deser, C**, **Fischer, C**, **Fox-Kemper, B**, **Kay, JE**, **Kinnison, D**, **Kushner, PJ**, **Larson, VE**, **Long, MC**, **Mickelson, S**, **Moore, JK**, **Nienhouse, E**, **Polvani, L**, **Rasch, PJ**, **Strand, WG.** 2020. The Community Earth System Model Version 2 (CESM2). *Journal of Advances in Modeling Earth Systems* **12**(2): e2019MS001916. DOI: https://doi.org/10.1029/2019MS001916.

Frey, KE, **Perovich, DK**, **Light, B.** 2011. The spatial distribution of solar radiation under a melting Arctic sea ice cover. *Geophysical Research Letters* **38**: L22501. DOI: https://doi.org/10.1029/2011GL049421.

Grenfell, TC. 1991. A radiative transfer model for sea ice with vertical structure variations. *Journal of Geophysical Research* **96**: 16991–17001.

Grenfell, TC, **Maykut, GA.** 1977. The optical properties of ice and snow in the Arctic Basin. *Journal of Glaciology* **18**: 445–463.

Grenfell, TC, **Perovich, DK**. 1984. Spectral albedos of sea ice and incident solar irradiance in the southern Beaufort Sea. *Journal of Geophysical Research: Oceans* **89**: 3573–3580.

Hunke, EC, **Lipscomb, WH**, **Turner, AK**, **Jeffery, N**, **Elliott, S.** 2015. CICE: The Los Alamos Sea Ice Model. Documentation and Software User's Manual Version 5.1. Los Alamos, NM: T-3 Fluid Dynamics Group, Los Alamos National Laboratory. Tech. Rep. LA-CC-06-012.

Itkin, P, **Hendricks, S**, **Webster, M**, **von Albedyll, L**, **Arndt, S**, **Divine, D**, **Jaggi, M**, **Oggier, M**, **Raphael, I**, **Ricker, R**, **Rohde, J**, **Schneebeli, M**, **Liston, GE.** 2023. Sea ice and snow characteristics from year-long transects at the MOSAiC Central Observatory. *Elementa: Science of the Anthropocene* **11**(1): 00048. DOI: https://doi.org/10.1525/elementa.2022.00048.

Jäkel, E, **Becker, S**, **Sperzel, TR**, **Niehaus, H**, **Spreen, G**, **Tao, R**, **Nicolaus, M**, **Dorn, W**, **Rinke, A**, **Brauchle, J**, **Wendisch, M.** 2024. Observations and modeling of areal surface albedo and surface types in the

Arctic. *The Cryosphere* **18**: 1185–1205. DOI: https://doi.org/10.5194/tc-18-1185-2024.

Jensen, JLWV. 1906. Sur les fonctions convexes et les inégalités entre les valeurs moyennes. *Acta Mathematica* **30**(1): 175–193. DOI: https://doi.org/10.1007/BF02418571.

Katlein, C, **Arndt, S**, **Belter, HJ**, **Castellani, G**, **Nicolaus, M.** 2019. Seasonal evolution of light transmission distributions through Arctic sea ice. *Journal of Geophysical Research: Oceans* **124**: 5418–5435. DOI: https://doi.org/10.1029/2018JC014833

Katlein, C, **Arndt, S**, **Nicolaus, M**, **Perovich, DK**, **Jakuba, MV**, **Suman, S**, **Elliott, S**, **Whitcomb, L**, **McFarland, C**, **Gerdes, R**, **Boetius, A**, **German, C.** 2015. Influence of ice thickness and surface properties on light transmission through Arctic sea ice. *Journal of Geophysical Research Oceans* **120**: 5932–5944. DOI: https://doi.org/10.1002/2015JC010914.

Light, B, **Maykut, G**, **Grenfell, T.** 2003. A two-dimensional Monte Carlo model of radiative transfer in sea ice. *Journal of Geophysical Research* **108**(C7): 3219. DOI: https://doi.org/10.1029/2002JC001513.

Light, B, **Grenfell, T**, **Perovich, D.** 2008. Transmission and absorption of solar radiation by Arctic sea ice during the melt season. *Journal of Geophysical Research* **113**: C03023. DOI: https://doi.org/10.1029/2006JC003977.

Light, B, **Smith, MM**, **Perovich, DK**, **Webster, MA**, **Holland, MM**, **Linhardt, F**, **Raphael, IA**, **Clemens-Sewall, D**, **Macfarlane, AR**, **Anhaus, P**, **Bailey, DA.** 2022. Arctic sea ice albedo: Spectral composition, spatial heterogeneity, and temporal evolution observed during the MOSAiC drift. *Elementa: Science of the Anthropocene* **10**(1). DOI: https://doi.org/10.1525/elementa.2021.000103.

Light, B, **Perovich, DK**, **Webster, MA**, **Polashenski, C**, **Dadic, R.** 2015. Optical properties of melting first-year Arctic sea ice. *Journal of Geophysical Research Oceans* **120**: 7657–7675. DOI: https://doi.org/10.1002/2015JC011163.

Macfarlane, AR, **Dadic, R**, **Smith, MM**, **Light, B**, **Nicolaus, M**, **Henna-Reetta, H**, **Webster, M**, **Linhardt, F**, **Hämmerle, S**, **Schneebeli, M.** 2023. Evolution of the microstructure and reflectance of the surface scattering layer on melting, level Arctic sea ice. *Elementa: Science of the Anthropocene* **11**: 1. DOI: https://doi.org/10.1525/elementa.2022.00103.

Meier, WN, **Fetterer, F**, **Savoie, M**, **Mallory, S**, **Duerr, R**, **Stroeve, J.** 2017. NOAA/NSIDC Climate Data Record of Passive Microwave Sea Ice Concentration, Version 3. Boulder, CO: NSIDC: National Snow and Ice Data Center. DOI: https://doi.org/10.7265/N59P2ZTG. Accessed July 2024.

Nicolaus, M, **Katlein, C**, **Maslanik, J**, **Hendricks, S.** 2012. Changes in Arctic sea ice result in increasing light transmittance and absorption. *Geophysical Research Letters* **39**(24): L24501. DOI: https://doi.org/10.1029/2012GL053738.

Nicolaus, M, **Perovich, DK**, **Spreen, G**, **Granskog, MA**, **von Albedyll, LV**, **Angelopoulos, M**, **Anhaus, P**, **Arndt, S**, **Belter, HJ**, **Bessonov, V**, **Birnbaum, G**, **Brauchle, J**, **Calmer, R**, **Cardellach, E**, **Cheng, B**, **Clemens-Sewall, D**, **Dadic, R**, **Damm, E**, **de Boer, G**, **Demir, O**, **Dethloff, K**, **Divine, DV**, **Fong, AA**, **Fons, S**, **Frey, MM**, **Fuchs, N**, **Gabarró, C**, **Gerland, S**, **Goessling, HF**, **Gradinger, R**, **Haapala, J**, **Haas, C**, **Hamilton, J**, **Hannula, H-R**, **Hendricks, S**, **Herber, A**, **Heuzé, C**, **Hoppmann, M**, **Høyland, KV**, **Huntemann, M**, **Hutchings, JK**, **Hwang, B**, **Itkin, P**, **Jacobi, H-W**, **Jaggi, M**, **Jutila, A**, **Kaleschke, L**, **Katlein, C**, **Kolabutin, N**, **Krampe, D**, **Kristensen, SS**, **Krumpen, T**, **Kurtz, N**, **Lampert, A**, **Lange, BA**, **Lei, R**, **Light, B**, **Linhardt, F**, **Liston, GE**, **Loose, B**, **Macfarlane, AR**, **Mahmud, M**, **Matero, IO**, **Maus, S**, **Morgenstern, A**, **Naderpour, R**, **Nandan, V**, **Niubom, A**, **Oggier, M**, **Oppelt, N**, **Pätzold, F**, **Perron, C**, **Petrovsky, T**, **Pirazzini, R**, **Polashenski, C**, **Rabe, B**, **Raphael, IA**, **Regnery, J**, **Rex, M**, **Ricker, R**, **Riemann-Campe, K**, **Rinke, A**, **Rohde, J**, **Salganik, E**, **Scharien, RK**, **Schiller, M**, **Schneebeli, M**, **Semmling, M**, **Shimanchuk, E**, **Shupe, MD**, **Smith, MM**, **Smolyanitsky, V**, **Sokolov, V**, **Stanton, T**, **Stroeve, J**, **Thielke, L**, **Timofeeva, A**, **Tonboe, RT**, **Tavri, A**, **Tsamados, M**, **Wagner, DN**, **Watkins, D**, **Webster, M**, **Wendisch, M.** 2022. Overview of the MOSAiC expedition: Snow and sea ice. *Elementa: Science of the Anthropocene* **10**(1): 00046. DOI: http://dx.doi.org/10.1525/elementa.2021.000046.

Patzold, F, **Bretschneider, L**, **Nowak, S**, **Brandt, B**, **Schlerf, A**, **Asmussen, MO**, **Bollmann, S**, **Barfuss, K**, **Harm-Altstadter, B**, **Hecker, P**, **Wehner, B**, **van der Wall, BG**, **Sachs, T**, **Huntrieser, H**, **Roiger, A**, **Lampert, A.** 2023. HELiPOD—Revolution and evolution of a helicopter-borne measurement system for multidisciplinary research in demanding environments. *Elementa: Science of the Anthropocene* **11**(1): 00031. DOI: https://doi.org/10.1525/elementa.2023.00031.

Pegau, WS, **Paulson, CA.** 2001. The albedo of Arctic leads in summer. *Annals of Glaciology* **33**: 221–224.

Perovich, D, **Raphael, I**, **Moore, R**, **Clemens-Sewall, D**, **Lei, R**, **Sledd, A**, **Polashenski, C.** 2023. Sea ice heat and mass balance measurements from four autonomous buoys during the MOSAiC drift campaign. *Elementa: Science of the Anthropocene* **11**(1): 00017. DOI: https://doi.org/10.1525/elementa.2023.00017.

Perovich, DK. 1990. Theoretical estimates of light reflection and transmission by spatially complex and temporally varying sea ice covers. *Journal of Geophysical Research* **95**: 9557–9567.

Perovich, DK. 2005. On the aggregate-scale partitioning of solar radiation in Arctic sea ice during the Surface Heat Budget of the Arctic Ocean (SHEBA) field experiment. *Journal of Geophysical Research* **110**(C3). DOI: https://doi.org/10.1029/2004JC002512.

Perovich, DK, **Grenfell, TC**, **Light, B**, **Hobbs, PV.** 2002. Seasonal evolution of the albedo of multiyear Arctic sea ice. *Journal of Geophysical Research: Oceans*. DOI: https://doi.org/10.1029/2000JC000438.

Pohl, C, Istomina, L, Tietsche, S, Jäkel, E, Stapf, J, Spreen, G, Heygster, G. 2020. Broadband albedo of Arctic sea ice from MERIS optical data. *The Cryosphere* **14**: 165–182. DOI: https://doi.org/10.5194/tc-14-165-2020.

Rabe, B, Cox, CJ, Fang, Y-C, Goessling, H, Granskog, MA, Hoppmann, M, Hutchings, JK, Krumpen, T, Kuznetsov, I, Lei, R, Li, T, Maslowski, W, Nicolaus, M, Perovich, D, Persson, O, Regnery, J, Rigor, I, Shupe, MD, Sokolov, V, Spreen, G, Stanton, T, Watkins, DM, Blockley, E, Buenger, HJ, Cole, S, Fong, A, Haapala, J, Heuzé, C, Hoppe, CJM, Janout, M, Jutila, A, Katlein, C, Krishfield, R, Lin, L, Ludwig, V, Morgenstern, A, O'brien, J, Zurita, AQ, Rackow, T, Riemann-Campe, K, Rohde, J, Shaw, W, Smolyanitsky, V, Solomon, A, Sperling, A, Tao, R, Toole, J, Tsamados, M, Zhu, J, Zuo, G. 2024. The MOSAiC distributed network: Observing the coupled Arctic system with multidisciplinary, coordinated platforms. *Elementa: Science of the Anthropocene* **12**(1): 00103. DOI: https://doi.org/10.1525/elementa.2023.00103.

Ran, T, Nicolaus, M, Katlein, C, Anhaus, P, Hoppmann, M, Spreen, G, Niehaus, H, Jäkel, E, Wendisch, M, Haas, C. 2024. Seasonality of spectral radiative fluxes and optical properties of Arctic sea ice during the spring–summer transition. *Elementa: Science of the Anthropocene* **12**(1): 00130. DOI: https://doi.org/10.1525/elementa.2023.00130.

Rantanen, M, Karpechko, AY, Lipponen, A, Nordling, K, Hyvärinen, O, Ruosteenoja, K, Vihma, T, Laaksonen, A. 2022. The Arctic has warmed nearly four times faster than the globe since 1979. *Communications Earth & Environment* **3**(1): 168.

Riihelä, A, Bright, RM, Anttila, K. 2021. Recent strengthening of snow and ice albedo feedback driven by Antarctic sea-ice loss. *Nature Geoscience* **14**: 832–836. DOI: https://doi.org/10.1038/s41561-021-00841-x.

Shupe, MD, Rex, M, Blomquist, B, Persson, POG, Schmale, J, Uttal, T, Althausen, D, Angot, H, Archer, S, Bariteau, L, Beck, I, Bilberry, J, Bucci, S, Buck, C, Boyer, M, Brasseur, Z, Brooks, IM, Calmer, R, Cassano, J, Castro, V, Chu, D, Costa, D, Cox, CJ, Creamean, J, Crewell, S, Dahlke, S, Damm, E, de Boer, G, Deckelmann, H, Dethloff, K, Dütsch, M, Ebell, K, Ehrlich, A, Ellis, J, Engelmann, R, Fong, AA, Frey, MM, Gallagher, MR, Ganzeveld, L, Gradinger, R, Graeser, J, Greenamyer, V, Griesche, H, Griffiths, S, Hamilton, J, Heinemann, G, Helmig, D, Herber, A, Heuzé, C, Hofer, J, Houchens, T, Howard, D, Inoue, J, Jacobi, H-W, Jaiser, R, Jokinen, T, Jourdan, O, Jozef, G, King, W, Kirchgaessner, A, Klingebiel, M, Krassovski, M, Krumpen, T, Lampert, A, Landing, W, Laurila, T, Lawrence, D, Lonardi, M, Loose, B, Lüpkes, C, Maahn, M, Macke, A, Maslowski, W, Marsay, C, Maturilli, M, Mech, M, Morris, S, Moser, M, Nicolaus, M, Ortega, P, Osborn, J, Pätzold, F, Perovich, DK, Petäjä, T, Pilz, C, Pirazzini, R, Posman, K, Powers, H, Pratt, KA, Preußer, A, Quéléver, L, Radenz, M, Rabe, B, Rinke, A, Sachs, T, Schulz, A, Siebert, H, Silva, T, Solomon, A, Sommerfeld, A, Spreen, G, Stephens, M, Stohl, A, Svensson, G, Uin, J, Viegas, J, Voigt, C, von der Gathen, P, Wehner, B, Welker, JM, Wendisch, M, Werner, M, Xie, ZQ, Yue, F. 2022. Overview of the MOSAiC expedition: Atmosphere. *Elementa: Science of the Anthropocene* **10**(1): 00060. DOI: https://doi.org/10.1525/elementa.2021.00060.

Smith, RC, Baker, KS. 1981. Optical properties of the clearest natural waters (200–899 nm). *Applied Optics* **20**: 177–184.

Smith, MM, Light, B, Macfarlane, AR, Perovich, DK, Holland, MM, Shupe, MD. 2022. Sensitivity of the Arctic sea ice cover to the summer surface scattering layer. *Geophysical Research Letters* **49**(9): e2022GL098349. DOI: https://doi.org/10.1029/2022GL098349.

Stroeve, JC, Veyssiere, G, Nab, C, Light, B, Perovich, D, Laliberté, J, Campbell, K, Landy, J, Mallett, R, Barrett, A, Liston, GE, Haddon, A, Wilkinson, J. 2024. Mapping potential timing of ice algal blooms from satellite. *Geophysical Research Letters* **51**(8): e2023GL106486. DOI: https://doi.org/10.1029/2023GL106486.

Stamnes, K, Hamre, B, Stamnes, S, Chen, N, Fan, Y, Li, W, Lin, Z, Stamnes, J. 2018. Progress in forward-inverse modeling based on radiative transfer tools for coupled atmosphere-snow/ice-ocean systems: A review and description of the AccuRT model. *Applied Sciences* **8**(12): 2682. DOI: https://doi.org/10.3390/app8122682.

Tao, R, Nicolaus, M, Katlein, C, Anhaus, P, Hoppmann, M, Spreen, G, Niehaus, H, Jäkel, E, Wendisch, M, Haas, C. 2024. Seasonality of spectral radiative fluxes and optical properties of Arctic sea ice during the spring–summer transition. *Elementa: Science of the Anthropocene* **12**(1): 00130. DOI: https://doi.org/10.1525/elementa.2023.00130.

Wang, C, Granskog, MA, Gerland, S, Hudson, SR, Perovich, DK, Nicolaus, M, Karlsen, TI, Fossan, K, Bratrein, M. 2014. Autonomous observations of solar energy partitioning in first-year sea ice in the Arctic Basin. *Journal of Geophysical Research Oceans* **119**: 2066–2080. DOI: https://doi.org/10.1002/2013JC009459.

Warren, SG, Brandt, RE. 2008. Optical constants of ice from the ultraviolet to the microwave: A revised compilation. *Journal of Geophysical Research* **113**(D14). DOI: https://doi.org/10.1029/2007JD009744.

Warren, SG. 2019. Optical properties of ice and snow. *Philosophical Transactions Royal Society A* **377**: 20180161. DOI: https://doi.org/10.1098/rsta.2018.0161.

Webster, M, Holland, M, Wright, N, Hendricks, S, Hutter, N, Itkin, P, Light, B, Lindhardt, F, Perovich, D, Raphael, I, Smith, M, von Albedyll, L, Zhang, J. 2022. Characterizing the spatial and temporal evolution of surface conditions of a melting Arctic sea ice cover. *Elementa Science of the Anthropocene* **10**(1): 000072. DOI: https://doi.org/10.1525/elementa.2021.000072.

How to cite this article: Perovich, D, Light, B, Smith, MM, Webster, M, Holland, MM, Clemens-Sewall, D, Raphael, IA, Polashenski, C, Barrett, AP, Cox, CJ, Itkin, P, Linhardt, F, Macfarlane, AR, Nicolaus, M, Oppelt, N, Shupe, MD, Stroeve, J, Tao, R. 2025. Theoretical estimates of light transmittance at the MOSAiC Central Observatory. *Elementa: Science of the Anthropocene* 13(1). DOI: https://doi.org/10.1525/elementa.2024.00076

Domain Editor-in-Chief: Jody W. Deming, University of Washington, Seattle, WA, USA

Guest Editor: Gunnar Spreen, Institute of Environmental Physics, University of Bremen, Bremen, Germany

Knowledge Domain: Ocean Science

Part of an Elementa Special Feature: The Multidisciplinary Drifting Observatory for the Study of Arctic Climate (MOSAiC)

Published: July 22, 2025 **Accepted:** June 7, 2025 **Submitted:** October 28, 2024

ELEMENTA
Science of the Anthropocene

Elem Sci Anth is a peer-reviewed open access
journal published by University of California Press.

OPEN ACCESS